

Task-Driven Subspace Decomposition for Knowledge Sharing and Isolation in LoRA-based Continual Learning

Lingfeng He¹ De Cheng¹ Huaijie Wang¹ Xi Yang¹ Nannan Wang¹ Xinbo Gao¹

Abstract

Continual Learning (CL) requires models to sequentially adapt to new tasks without forgetting old knowledge. Recently, Low-Rank Adaptation (LoRA), a representative Parameter-Efficient Fine-Tuning (PEFT) method, has gained increasing attention in CL. Several LoRA-based CL methods reduce interference across tasks by separating their update spaces, typically building the new space from the estimated null space of past tasks. However, they (i) overlook task-shared directions, which suppresses knowledge transfer, and (ii) fail to capture truly effective task-specific directions since these “null bases” of old tasks can remain nearly inactive for new task under correlated tasks. To address this, we study LoRA learning capability from a projection energy perspective, and propose Low-rank Decomposition and Adaptation (LoDA). It performs a task-driven decomposition to build general and truly task-specific LoRA subspaces by solving two energy-based objectives, decoupling directions for knowledge sharing and isolation. LoDA fixes LoRA down-projections on two subspaces and learns robust up-projections via a Gradient-Aligned Optimization (GAO) approach. After each task, before integrating the LoRA updates into the backbone, LoDA derives a closed-form recalibration for the general update, approximating a feature-level joint optimum along this task-shared direction. Experiments indicate that LoDA outperforms existing CL methods.

1. Introduction

Continual Learning (CL) studies how a model can continuously acquire new knowledge from a stream of tasks while retaining previously learned capabilities (Kirkpatrick et al., 2017; Qiu et al., 2025). A key challenge is the stability-plasticity dilemma (Kim & Han, 2023): the model must

¹Xidian University, Xi’an, China. Correspondence to: De Cheng <dcheng@xidian.edu.cn>.

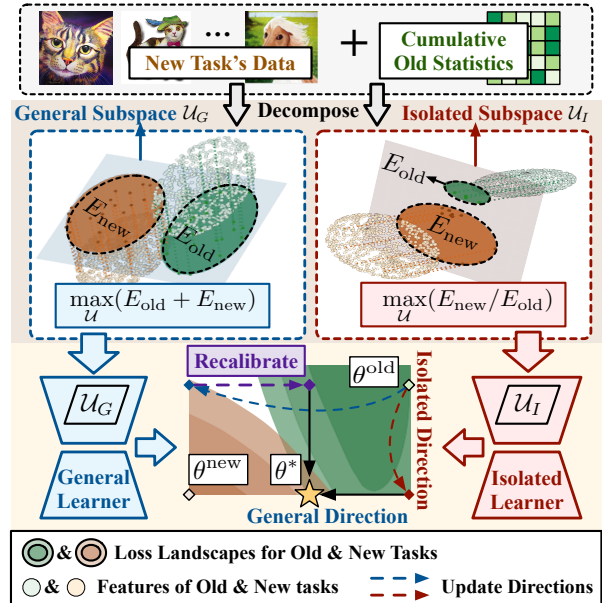


Figure 1. LoDA decomposes the update space into general & isolated subspaces (\mathcal{U}_G & \mathcal{U}_I) to fix LoRA down-projections. By updating in two subspaces with a post-hoc recalibration, it reaches θ^* in a shared low-loss region of old and new tasks. E_{old} and E_{new} denote the *subspace projection energy* of old and new features. Darker colors in the loss contour map denote lower values.

remain plastic enough to adapt to new tasks while keeping stable to avoid forgetting of learned knowledge. With the rise of Pre-Trained Models (PTMs), CL has shifted from training from scratch (Kirkpatrick et al., 2017; Wang et al., 2021) to sequentially adapting strong pre-learned representations. In this regime, Parameter-Efficient Fine-Tuning (PEFT)-based methods (Wang et al., 2022b; Smith et al., 2023; Tan et al., 2024) introduce lightweight trainable components for adaptation while preserving the generalization of the backbone, achieving remarkable CL performances.

Among various PEFT paradigms, Low-Rank Adaptation (LoRA) (Hu et al., 2022) emerged as a representative and widely-used approach due to its simplicity. It parameterizes the updates with two trainable low-rank matrices while keeping the pre-trained weights frozen. Several works (Zhu et al., 2025; Liang & Li, 2024) have explored LoRA for CL by explicitly isolating task-specific LoRA update subspaces to reduce cross-task interference and mitigate forgetting.

However, they face two limitations. Firstly, they mainly focus on subspace isolation, which can discard a large portion of general and transferable directions across tasks, thereby suppressing inter-task knowledge sharing. Secondly, they build the “isolated” subspace for the new task by seeking directions that are inactive on old tasks, typically from the estimated null space of old tasks (Liang & Li, 2024; Wang et al., 2023). But under correlated task distributions in realistic CL, the null spaces of past and new tasks can exhibit substantial overlap, meaning that the estimated isolated bases may still be nearly inactivated by the new task. As a result, they form a “safe zone” rather than a truly effective task-specific subspace. These limitations raise a key question: *how can we properly set LoRA subspaces to preserve transferable directions while learning truly task-specific knowledge, achieving a better stability-plasticity trade-off?*

To address this, we propose a Low-rank Decomposition and Adaptation (LoDA) framework for CL, which performs a task-driven decomposition and derives two LoRA subspaces for knowledge sharing and task isolation. We first reveal that *the impact of a LoRA update on the loss is governed by the projection energy of the task features onto the down-projection’s row subspace*. This motivates a data-driven design to freeze down-projections as a gate that selects learnable new feature components while controlling interference with past tasks. Guided by this, LoDA decomposes the update space into two down-projection subspaces using new data and cumulative old data statistics, as shown in Fig.1: (i) a *general subspace* \mathcal{U}_G that yields high projection energy across both old and new tasks ($\mathcal{U}_G = \arg \max_{\mathcal{U}} (E_{\text{old}} + E_{\text{new}})$), capturing directions salient across all tasks and enabling knowledge transfer; (ii) an *isolated subspace* \mathcal{U}_I that exhibit largest new-to-old relative energy ($\mathcal{U}_I = \arg \max_{\mathcal{U}} (E_{\text{new}}/E_{\text{old}})$), identifying updates effective for the new task with little impact on past tasks.

Based on the decomposition, LoDA builds a dual-branch LoRA module: each branch’s down-projection is fixed on decomposed subspace bases and the up-projection is learnable. To steer the learning of up-projections toward robust and cross-class conflict-free directions, we design Gradient-Aligned Optimization (GAO) that encourages its gradient consistency across label-disjoint subsets. After each task, LoDA integrate the decoupled updates into the backbone: (i) Since the general update inevitably induces feature drift of old tasks when learning the new task, we derive a closed-form rescaling matrix to recalibrate it by minimizing feature optimization errors on all tasks to approximate a joint optimum; (ii) Since the isolated update incurs little interference on past tasks, we directly merge it into the backbone.

Our main contributions can be summarized as follows:

- We propose a task-driven decomposition that con-

structs general and truly isolated down-projection subspaces based on the feature projection energy, decoupling directions for knowledge sharing and isolation.

- We propose LoDA, a dual-branch LoRA framework that fixes down-projections on task-driven bases and learns robust up-projections via GAO, with a post-hoc closed-form recalibration for the general branch.
- Experiments demonstrate that LoDA outperforms existing PEFT-based CL methods on multiple benchmarks.

2. Related Works

PEFT-based Continual Learning. PEFT-based CL methods typically keep a pre-trained model frozen and insert lightweight learnable modules for continual adaptation. Prompt pool-based methods (Wang et al., 2022b; Smith et al., 2023; Gao et al., 2024) build a set of learnable prompts and update relevant prompts during each session to encode task-specific knowledge. PGP (Qiao et al., 2023) and VPT-NSP (Lu et al., 2024) further theoretically deduce anti-forgetting conditions for visual prompts and constrain their updates via gradient projection.

Recently, LoRA-based approaches gain increasing attention. SD-LoRA (Wu et al., 2025b) separates the learning of directions and magnitudes to update parameters within a low-loss path. Some methods design regularization schemes for LoRA to mitigate forgetting. O-LoRA (Wang et al., 2023) and InfLoRA (Liang & Li, 2024) constrain LoRA updates to estimated null space of previous tasks, thereby minimizing past output change when learning new tasks. BiLoRA (Zhu et al., 2025) and PLAN (Wang et al., 2025) impose fixed orthogonal bases on LoRA down-projections, restricting the updates to pre-defined subspace and reducing cross-task interference. However, such orthogonal constraints may fail to uncover truly isolated subspaces while discarding task-shared directions, limiting stability-plasticity trade-off.

Model Merging. Model merging (Ilharco et al., 2023; Ortiz-Jimenez et al., 2023) aims to integrate weights trained on different tasks into a single network. Some works (Stoica et al., 2025; Gargiulo et al., 2025) factorize task-wise updates in singular directions and combine them to reduce task interference. Several works have extended this idea to CL. Connector (Lin et al., 2022) designs a convex combination for stability- and plasticity-oriented weights. CoMA (Marouf et al., 2024) designs an EMA-style merging for old and new weights and enhances it with Fisher matrix. BECAME (Li et al., 2025b) models loss changes induced by merging and derives optimal merging coefficients. They mainly rely on local linearity assumptions and gradient-based estimates, leading to approximation errors. We design a feature-level objective and deduce an exact optimum, avoiding such error.

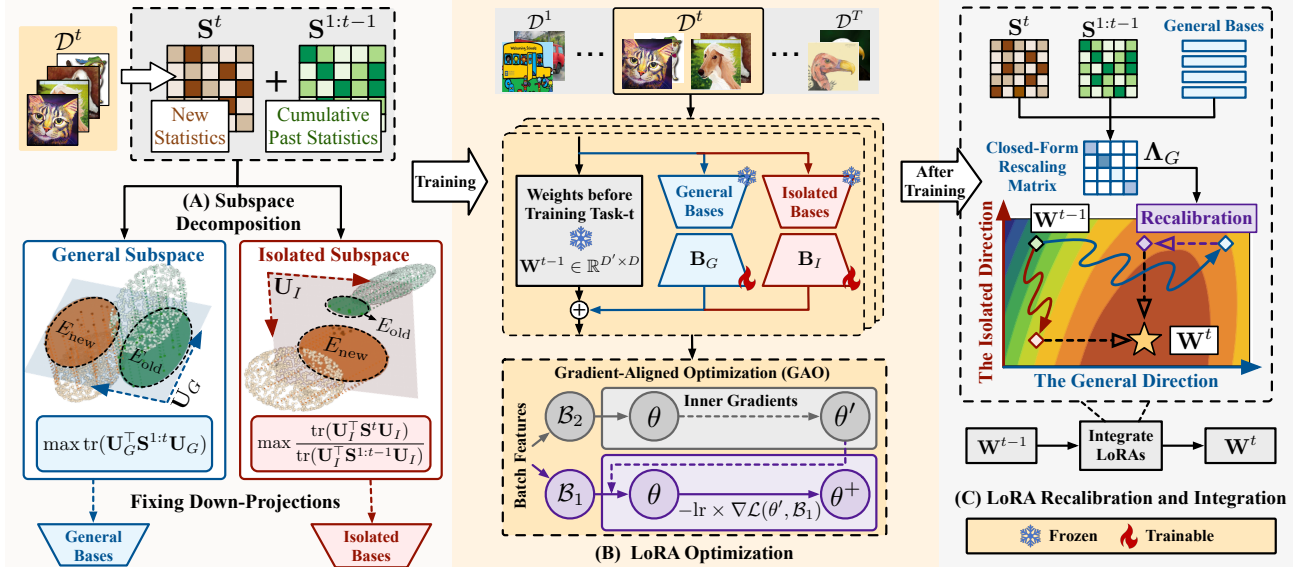


Figure 2. Overall framework. At Task- t , we freeze backbone weight \mathbf{W}^{t-1} and insert a dual-branch LoRA module. (A) We decompose the update space into general & isolated subspaces for LoRA down-projections. (B) Then we freeze down-projections and train up-projections on \mathcal{D}^t via GAO. (C) After training, the LoRA updates are integrated into backbone with a recalibration on the general branch.

3. Methodology

Problem Definition. In CL, there are T sequential tasks with non-overlapping classes. The datasets are defined as $\{\mathcal{D}^1, \dots, \mathcal{D}^t, \dots, \mathcal{D}^T\}$. $\mathcal{D}^t = \{\mathbf{x}_i^t, y_i^t\}_{i=1}^{N^t}$ denotes the t -th task’s dataset, where $\mathbf{x}_i^t \in \mathbb{R}^{H \times W \times C}$ is the i -th input and $y_i^t \in \mathcal{Y}^t$ is its class label. \mathcal{Y}^t denotes the label space of the t -th task, and $\mathcal{Y}^t \cap \mathcal{Y}^{t'} = \emptyset$ for $t \neq t'$. The objective of CL is to train a model $f(\theta, \cdot)$ sequentially on T tasks and performs well on all seen classes $\mathcal{Y}^1 \cup \dots \cup \mathcal{Y}^T$.

Overall framework. An overview of the proposed method is shown in Fig. 2. Following existing PEFT-based methods (Wang et al., 2022b; Tan et al., 2024), we use a pre-trained Vision Transformer (ViT) (Dosovitskiy et al., 2021) as backbone. At the t -th task, for each ViT layer, we freeze the backbone weights \mathbf{W}^{t-1} and attach a dual-branch LoRA module, including a general branch for knowledge sharing and an isolated branch to learn task-specific updates. Guided by our gradient analysis in Sec. 3.1, a task-driven subspace decomposition (Fig. 2(A)) is proposed to derive the general and isolated subspace bases via two projection-energy-based objectives. We freeze each branch’s down-projection on the decomposed subspace bases, and then learn robust up-projection on \mathcal{D}^t via a Gradient-Aligned Optimization (GAO) approach, which encourages gradient consistency across label-disjoint subsets (Fig. 2(B)). After each task, we integrate the LoRA updates into the backbone weight. The general branch is recalibrated by a closed-form rescaling matrix Λ_G to approximate a feature-level joint optimum, while the isolated branch is directly merged (Fig. 2(C)).

3.1. LoRA Analysis when Fixing Down-Projections

Given the backbone weight $\mathbf{W}^{t-1} \in \mathbb{R}^{D' \times D}$ before the t -th task, where D and D' are the input and output dimensions. LoRA trains a low-rank update parameterized by two matrices $\mathbf{A} \in \mathbb{R}^{r \times D}$ and $\mathbf{B} \in \mathbb{R}^{D' \times r}$, while keeping \mathbf{W}^{t-1} fixed. For an input $\mathbf{X} \in \mathbb{R}^D$, the layer output is given by:

$$\mathbf{Y} = \mathbf{X}(\mathbf{W}^{t-1} + \mathbf{B}\mathbf{A})^\top \in \mathbb{R}^{D'}. \quad (1)$$

Theorem 3.1. Let $\mathcal{L}(\mathbf{Y})$ be a differentiable loss for \mathbf{Y} . Fix \mathbf{A} and update only \mathbf{B} by one gradient descent step $\mathbf{B}' = \mathbf{B} - \eta \frac{\partial \mathcal{L}}{\partial \mathbf{B}}$. Then the first-order update $\Delta \mathbf{Y}$ of \mathbf{Y} and the loss decrease is gated by the projected energy $E = \|\mathbf{A}\mathbf{X}^\top\|_2^2$:

$$\begin{aligned} \Delta \mathbf{Y} &\triangleq \mathbf{Y}' - \mathbf{Y} = -\eta \|\mathbf{A}\mathbf{X}^\top\|_2^2 \frac{\partial \mathcal{L}}{\partial \mathbf{Y}}, \\ \mathcal{L}(\mathbf{Y}') - \mathcal{L}(\mathbf{Y}) &= -\eta \|\mathbf{A}\mathbf{X}^\top\|_2^2 \left\| \frac{\partial \mathcal{L}}{\partial \mathbf{Y}} \right\|_2^2 + o(\|\Delta \mathbf{Y}\|). \end{aligned} \quad (2)$$

If the rows of \mathbf{A} are orthonormal ($\mathbf{A}\mathbf{A}^\top = \mathbf{I}_r$ and \mathbf{I}_r is the $r \times r$ identity matrix), $\|\mathbf{A}\mathbf{X}^\top\|_2^2$ is the squared Euclidean norm of the projection of \mathbf{X} onto the row space of \mathbf{A} .

Discussion. Theorem 3.1 reveals: (1) Updating \mathbf{B} changes the output \mathbf{Y} exactly along the steepest descent direction $-\frac{\partial \mathcal{L}}{\partial \mathbf{Y}}$; (2) The magnitude of this change is modulated by the projection energy $E = \|\mathbf{A}\mathbf{X}^\top\|_2^2$, which quantifies how much the input feature \mathbf{X} lies in the subspace selected by \mathbf{A} .

3.2. Low-Rank Subspace Decomposition

Theorem 3.1 indicates that the LoRA’s learning capacity is determined by the magnitude of \mathbf{X} ’s component in the sub-

space spanned by \mathbf{A} . This motivates controlling plasticity on new data and interference with past tasks by designing the down-projection \mathbf{A} in a task-driven manner. Following this, we introduce a dual-branch LoRA with complementary roles, consisting of a general branch LoRA $_G$ (matrices $\mathbf{A}_G, \mathbf{B}_G$) and an isolated branch LoRA $_I$ (matrices $\mathbf{A}_I, \mathbf{B}_I$):

$$\mathbf{Y} = \mathbf{X}(\mathbf{W}^{t-1} + w_G \mathbf{B}_G \mathbf{A}_G + \mathbf{B}_I \mathbf{A}_I)^\top, \quad (3)$$

where w_G is a hyper-parameter weighting the contribution of two branches. We fix \mathbf{A}_G and \mathbf{A}_I and build them via a data-driven low-rank decomposition of the current feature space: \mathbf{A}_G spans a **general subspace** $\mathcal{U}_G \triangleq \text{span}(\mathbf{U}_G)$ that aligns with dominant directions accumulated from all tasks to enable knowledge sharing and inter-task transfer, while \mathbf{A}_I spans an **isolated subspace** $\mathcal{U}_I \triangleq \text{span}(\mathbf{U}_I)$ that is strongly activated by the current task but weakly activated by past tasks, isolating task-specific update directions.

General Subspace Bases. Let $\mathbf{X}^i \in \mathbb{R}^{(N^i N^p) \times D}$ denote the concatenated input of task i , where N^p denote the number of patch tokens per sample. Let $\mathbf{S}^i \triangleq \mathbf{X}^{i\top} \mathbf{X}^i \in \mathbb{R}^{D \times D}$ denote the second-moment statistics, and $\mathbf{S}^{1:t-1} \triangleq \sum_{i=1}^{t-1} \mathbf{S}^i$ denote the accumulated past statistics. To build a rank- r general subspace, we seek r orthonormal bases \mathbf{U}_G such that the overall projection energy ($E_{\text{old}} + E_{\text{new}}$) of both old and new tasks onto $\mathcal{U}_G = \text{span}(\mathbf{U}_G)$ is maximized:

$$\begin{aligned} \mathbf{U}_G &= \arg \max_{\mathbf{U}^\top \mathbf{U} = \mathbf{I}_r} \left(\underbrace{\|\mathbf{X}^t \mathbf{U}\|_F^2}_{E_{\text{new}}} + \underbrace{\sum_{i=1}^{t-1} \|\mathbf{X}^i \mathbf{U}\|_F^2}_{E_{\text{old}}} \right) \\ &= \arg \max_{\mathbf{U}^\top \mathbf{U} = \mathbf{I}_r} \text{tr}(\mathbf{U}^\top \mathbf{S}^{1:t-1} \mathbf{U} + \mathbf{U}^\top \mathbf{S}^t \mathbf{U}), \end{aligned} \quad (4)$$

where $\text{tr}(\cdot)$ denotes the trace. Since the statistics satisfy $\mathbf{S}^{1:t-1} \succeq \mathbf{0}$ and $\mathbf{S}^t \succeq \mathbf{0}$, the solution is given by the top- r singular vectors of $(\mathbf{S}^{1:t-1} + \mathbf{S}^t)$, where $\mathbf{U}_G = \mathbf{U}_{S^{1:t-1} + \mathbf{S}^t}$ and $[\mathbf{U}_S, \Sigma_S, \mathbf{V}_S] = \text{SVD}(\mathbf{S}^{1:t-1} + \mathbf{S}^t)$. $\text{SVD}(\cdot)$ denotes the Singular Value Decomposition (SVD) operator. A brief derivation is provided in Appx.??.

Isolated Subspace Bases. Aiming to learn task-specific directions, we design an isolated subspace whose directions are strongly driven by task t but weakly driven by past tasks $1:t-1$. Prior works (Wang et al., 2021; Liang & Li, 2024; Lu et al., 2024) derive the bases by approximating the **null space** \mathbf{U}_{null} of old tasks, where $\sum_{i=1}^{t-1} \|\mathbf{X}^i \mathbf{U}_{\text{null}}\| \approx 0$. However, real-world task streams can be highly correlated in representation space, and the estimated null space of past tasks can also be nearly inactive for the new task, leading to a small projection $\|\mathbf{X}^t \mathbf{U}_{\text{null}}\|$ and suboptimal subspace isolation. We empirically verify this issue on a challenging yet representative CL benchmark 10S-ImageNetA. We measure how much the new-task inputs project onto the previous-task null space \mathbf{U}_{null} . We define the **relative projection energy**

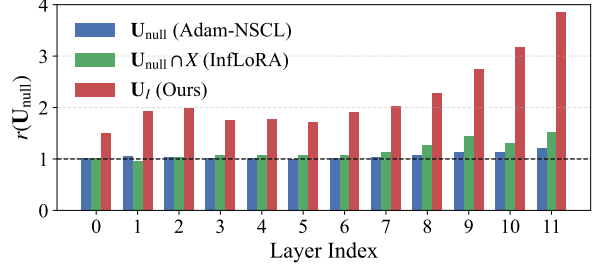


Figure 3. Averaged $r^t(\mathbf{U}_{\text{null}})$ in different layers on ImageNetA.

$r^t(\mathbf{U}_{\text{null}})$ of \mathbf{U}_{null} on task t against all past tasks $1:t-1$ as:

$$r^t(\mathbf{U}_{\text{null}}) \triangleq \frac{\|\mathbf{X}^t \mathbf{U}_{\text{null}}\|_F^2 / \|\mathbf{X}^t\|_F^2}{\sum_{i=1}^{t-1} \|\mathbf{X}^i \mathbf{U}_{\text{null}}\|_F^2 / (\sum_{i=1}^{t-1} \|\mathbf{X}^i\|_F^2)}. \quad (5)$$

As illustrated in Fig. 3, $r^t(\mathbf{U}_{\text{null}})$ is close to 1.0, indicating that **the estimated null-space directions are activated to a similar extent by both the current and previous tasks**, and thus are not truly effective isolated bases for the new task.

Unlike these methods, we select the r -dimensional isolated directions $\mathbf{U}_I \in \mathbb{R}^{D \times r}$ by explicitly maximizing the ratio between (i) the projection energy E_{new} of task t and (ii) the accumulated energy E_{old} of all previous tasks $1:t-1$:

$$\begin{aligned} \mathbf{U}_I &= \arg \max_{\mathbf{U} \in \mathbb{R}^{D \times r}} \frac{\underbrace{\|\mathbf{X}^t \mathbf{U}\|_F^2}_{E_{\text{new}}}}{\underbrace{\left(\sum_{i=1}^{t-1} \|\mathbf{X}^i \mathbf{U}\|_F^2 \right)}_{E_{\text{old}}}} \\ &= \arg \max_{\mathbf{U} \in \mathbb{R}^{D \times r}} \frac{\text{tr}(\mathbf{U}^\top \mathbf{S}^t \mathbf{U})}{\text{tr}(\mathbf{U}^\top \mathbf{S}^{1:t-1} \mathbf{U})}. \end{aligned} \quad (6)$$

Theorem 3.2 (Computation of \mathbf{U}_I). *Since $\mathbf{S}^{1:t-1}$ is the Gram matrix of past features with a huge sample size $\sum_{i=1}^{t-1} N^i N^p \gg D$, we assume it is full rank thus $\mathbf{S}^{1:t-1} \succ \mathbf{0}$. Let $\mathbf{S}^{1:t-1} = \mathbf{L}\mathbf{L}^\top$ be its Cholesky factorization and define $\tilde{\mathbf{S}}^t \triangleq \mathbf{L}^{-1} \mathbf{S}^t (\mathbf{L}^{-1})^\top$. Then the optimal \mathbf{U}_I of (6) is*

$$\mathbf{U}_I = (\mathbf{L}^{-1})^\top \tilde{\mathbf{U}}_I,$$

where $\tilde{\mathbf{U}}_I \in \mathbb{R}^{D \times r}$ consists of **top- r singular vectors of $\tilde{\mathbf{S}}^t$** .

Proof. Using $\mathbf{S}^{1:t-1} = \mathbf{L}\mathbf{L}^\top$, we rewrite the objective as:

$$f(\mathbf{U}) = \frac{\text{tr}((\mathbf{L}^\top \mathbf{U})^\top \mathbf{L}^{-1} \mathbf{S}^t (\mathbf{L}^{-1})^\top (\mathbf{L}^\top \mathbf{U}))}{\text{tr}((\mathbf{L}^\top \mathbf{U})^\top (\mathbf{L}^\top \mathbf{U}))}. \quad (7)$$

Define $\tilde{\mathbf{S}}^t \triangleq \mathbf{L}^{-1} \mathbf{S}^t \mathbf{L}^{-\top}$ and make the substitution $\tilde{\mathbf{U}} \triangleq \mathbf{L}^\top \mathbf{U}$. Then Eq.7 can be formulated as follows:

$$f(\mathbf{U}) = \frac{\text{tr}(\tilde{\mathbf{U}}^\top \mathbf{L}^{-1} \mathbf{S}^t (\mathbf{L}^{-1})^\top \tilde{\mathbf{U}})}{\text{tr}(\tilde{\mathbf{U}}^\top \tilde{\mathbf{U}})} = \frac{\text{tr}(\tilde{\mathbf{U}}^\top \tilde{\mathbf{S}}^t \tilde{\mathbf{U}})}{\text{tr}(\tilde{\mathbf{U}}^\top \tilde{\mathbf{U}})}. \quad (8)$$

Since Eq.8 is invariant to the scale of $\tilde{\mathbf{U}}$ and depends only on the directions of $\tilde{\mathbf{U}}$, we impose the normalization $\tilde{\mathbf{U}}^\top \tilde{\mathbf{U}} = \mathbf{I}_r$ without loss of optimality. Then the objective becomes:

$$\max_{\tilde{\mathbf{U}} \in \mathbb{R}^{D \times r}} \text{tr}(\tilde{\mathbf{U}}^\top \tilde{\mathbf{S}}^t \tilde{\mathbf{U}}) \quad \text{s.t.} \quad \tilde{\mathbf{U}}^\top \tilde{\mathbf{U}} = \mathbf{I}_r. \quad (9)$$

The maximum is attained when the columns of $\tilde{\mathbf{U}}$ span the top- r singular vectors of $\tilde{\mathbf{S}}^t$, where $\tilde{\mathbf{U}}_I = \tilde{\mathbf{U}}_{S[:,1:r]}$ and $[\tilde{\mathbf{U}}_S, \tilde{\Sigma}_S, \tilde{\mathbf{V}}_S] = \text{SVD}(\tilde{\mathbf{S}}^t)$ similar to Eq.4. Finally, by substituting back $\tilde{\mathbf{U}} = \mathbf{L}^\top \mathbf{U}$, we derive $\mathbf{U}_I = (\mathbf{L}^{-1})^\top \tilde{\mathbf{U}}_I$. \square

3.3. LoRA Optimization

Anchoring Down-Projection Matrices. We initialize \mathbf{A}_G and \mathbf{A}_I using the derived low-rank subspace bases:

$$\mathbf{A}_G \leftarrow \mathbf{U}_G^\top, \quad \mathbf{A}_I \leftarrow \text{QR}(\mathbf{U}_I^\top), \quad (10)$$

where $\mathbf{U}_G \in \mathbb{R}^{D \times r}$ and $\mathbf{U}_I \in \mathbb{R}^{D \times r}$ are the bases of the general and isolated subspaces, respectively. $\text{QR}(\cdot)$ denotes the thin-QR factorization that returns the orthonormal factor, so that \mathbf{A}_I has orthonormal rows while preserving $\text{span}(\mathbf{A}_I) = \text{span}(\mathbf{U}_I)$ for stable optimization. \mathbf{A}_G and \mathbf{A}_I are then frozen throughout the optimization on \mathcal{D}^t .

Optimizing Up-Projection Matrices. After anchoring \mathbf{A}_G and \mathbf{A}_I , we further regularize the learnable parameters \mathbf{B}_G and \mathbf{B}_I to induce consistent gradients across diverse classes, so they generalize better and are less susceptible to interference from potential future classes. Specifically, we propose a within-task *Gradient-Aligned Optimization (GAO)* algorithm. Given a batch \mathcal{B} , we split it into two label-disjoint subsets \mathcal{B}_1 and \mathcal{B}_2 , GAO implicitly encourages their gradients to align by coupling their gradients. At each step, it first takes a normalized inner update on parameter θ using the gradient from one subset, and then conducts optimization on the other subset under the perturbed parameter:

$$\begin{aligned} \theta^+ &\leftarrow \theta - \eta \nabla_{\theta} \mathcal{L} \left(\theta - \rho \frac{\nabla_{\theta} \mathcal{L}(\theta, \mathcal{B}_2)}{\|\nabla_{\theta} \mathcal{L}(\theta, \mathcal{B}_2)\|_2}, \mathcal{B}_1 \right), \\ \theta^{++} &\leftarrow \theta^+ - \eta \nabla_{\theta} \mathcal{L} \left(\theta^+ - \rho \frac{\nabla_{\theta} \mathcal{L}(\theta^+, \mathcal{B}_1)}{\|\nabla_{\theta} \mathcal{L}(\theta^+, \mathcal{B}_1)\|_2}, \mathcal{B}_2 \right), \end{aligned} \quad (11)$$

where $\rho \sim \text{U}(0, \rho_{\max})$ is a randomized inner-step scale for robustness, and η is the learning rate. $\mathcal{L}(\theta, \mathcal{B})$ denotes the standard cross-entropy loss computed on \mathcal{B} . Intuitively, it enables learning one group under the gradient interference from another group, suppressing conflicting directions and promoting shared gradients across groups.

3.4. LoRA Recalibration and Integration

After training, we recalibrate LoRA_G via a closed-form matrix that minimizes feature optimization error over tasks $1:t$. We then merge updates of two branches into the backbone to reach a joint low-loss region for old and new tasks.

Since the general low-rank branch is designed to capture update directions that are highly activated by both the new task and previous tasks. Therefore, directly adding the optimal update for \mathcal{D}^t leads to uncontrolled representation drifts of

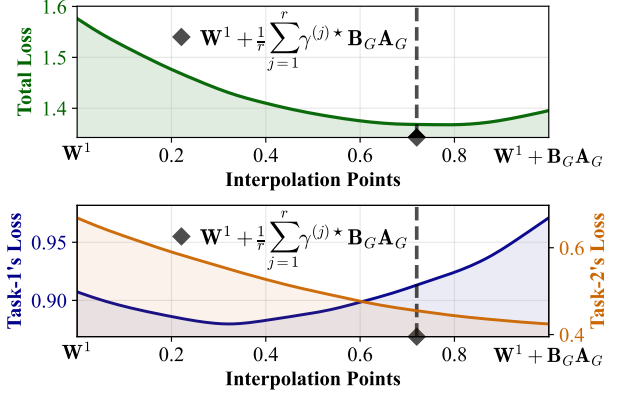


Figure 4. Loss values along the general direction (ImageNetA).

past tasks and causes forgetting. To address this, we derive an optimal factor to recalibrate each rank-1 unit in LoRA_G that minimizes feature-level optimization error. Firstly, we decompose the r -rank LoRA $\{\mathbf{B}_G, \mathbf{A}_G\}$ into r rank-1 units $\{\mathbf{B}_G^{(j)}, \mathbf{A}_G^{(j)}\}_{j=1}^r$, where $\mathbf{B}_G \mathbf{A}_G = \sum_{j=1}^r \mathbf{B}_G^{(j)} \mathbf{A}_G^{(j)}$. For each rank-1 unit, we replace its up-projection matrix $\mathbf{B}_G^{(j)}$ by an optimal $\mathbf{B}_G^{(j)*}$ that achieves the minimal optimization error of both the new task and all previous tasks. The objective of $\mathbf{B}_G^{(j)*}$ can be formulated as follows:

$$\begin{aligned} \min_{\mathbf{B}_G^{(j)*}} \quad & \lambda \left\| \mathbf{X}^t (\mathbf{B}_G^{(j)*} \mathbf{A}_G^{(j)})^\top - \mathbf{X}^t (\mathbf{B}_G^{(j)} \mathbf{A}_G^{(j)})^\top \right\|_F^2 \\ & + \sum_{i=1}^{t-1} \left\| \mathbf{X}^i (\mathbf{B}_G^{(j)*} \mathbf{A}_G^{(j)})^\top \right\|_F^2. \end{aligned} \quad (12)$$

The first term matches the LoRA outputs produced by $\mathbf{B}_G^{(j)*}$ to those produced by the current optimal unit $\mathbf{B}_G^{(j)}$ on the current task t . The second term regularizes $\mathbf{B}_G^{(j)*}$ by minimizing the joint feature optimization error induced by $\mathbf{B}_G^{(j)*}$ on all previous tasks $1:t-1$. λ is a hyper-parameter that balances errors on the new task \mathcal{D}^t and past tasks $\mathcal{D}^{1:t-1}$.

Theorem 3.3 (Closed-form solution for Eq.12). *Let $\mathbf{S}^t = \mathbf{X}^{t\top} \mathbf{X}^t \in \mathbb{R}^{D \times D}$ and $\mathbf{S}^{1:t} = \sum_{i=1}^{t-1} \mathbf{X}^i \mathbf{X}^{i\top} \in \mathbb{R}^{D \times D}$, the optimal solution of Eq.12 is given by:*

$$\mathbf{B}_G^{(j)*} = \frac{\lambda \mathbf{A}_G^{(j)} \mathbf{S}^t \mathbf{A}_G^{(j)\top}}{\mathbf{A}_G^{(j)} (\lambda \mathbf{S}^t + \mathbf{S}^{1:t-1}) \mathbf{A}_G^{(j)\top}} \mathbf{B}_G^{(j)}. \quad (13)$$

For each unit, this closed-form solution rescales the optimal weight $\mathbf{B}_G^{(j)}$ of the t -th task by a data-dependent factor $\gamma^{(j)*}$ without any approximations, where

$$\gamma^{(j)*} \triangleq \frac{\lambda \mathbf{A}_G^{(j)} \mathbf{S}^t \mathbf{A}_G^{(j)\top}}{\mathbf{A}_G^{(j)} (\lambda \mathbf{S}^t + \mathbf{S}^{1:t-1}) \mathbf{A}_G^{(j)\top}} \in [0, 1].$$

Discussion. We provide a toy example to show knowledge sharing in LoRA_G in Fig.4. We examine the losses along the general update by interpolating from \mathbf{W}^1 to

Task-Driven Subspace Decomposition for Knowledge Sharing and Isolation in LoRA-based Continual Learning

Table 1. Experimental results for 10 incremental tasks on ImageNetR, ImageNetA, CIFAR100, and CUB. We report the averaged results over 3 random seeds. The highest results are in **bold**, and the second highest results are underlined. “FR” denotes the use of feature replay.

Method	Venue	FR	10S-ImageNetR		10S-ImageNetA		10S-CIFAR100		10S-CUB	
			$\mathcal{A}_{Last} \uparrow$	$\mathcal{A}_{Avg} \uparrow$						
L2P (Wang et al., 2022b)	CVPR’22	✗	72.34 \pm 0.17	77.36 \pm 0.64	44.04 \pm 0.93	51.24 \pm 2.26	84.06 \pm 0.88	88.26 \pm 1.34	67.02 \pm 1.90	79.62 \pm 1.60
DualPrompt (Wang et al., 2022a)	ECCV’22	✗	69.10 \pm 0.62	74.28 \pm 0.66	53.19 \pm 0.74	64.59 \pm 0.08	86.93 \pm 0.24	91.13 \pm 0.32	68.48 \pm 0.47	80.59 \pm 1.50
CODAPrompt (Smith et al., 2023)	CVPR’23	✗	73.31 \pm 0.50	78.47 \pm 0.53	52.08 \pm 0.12	63.92 \pm 0.12	83.21 \pm 3.39	87.71 \pm 3.17	77.23 \pm 1.12	81.90 \pm 0.85
InfLoRA (Liang & Li, 2024)	CVPR’24	✗	74.75 \pm 0.64	80.67 \pm 0.55	49.20 \pm 1.12	60.92 \pm 0.61	86.75 \pm 0.35	91.72 \pm 0.15	70.82 \pm 0.23	81.39 \pm 0.14
SD-LoRA (Wu et al., 2025b)	ICLR’25	✗	77.34 \pm 0.35	82.04 \pm 0.24	55.96 \pm 0.73	64.95 \pm 1.63	88.01 \pm 0.31	92.54 \pm 0.18	77.48 \pm 0.20	85.59 \pm 0.44
Bi-LoRA (Zhu et al., 2025)	CVPR’25	✗	77.95 \pm 0.14	81.52 \pm 0.26	–	–	87.46 \pm 0.76	92.50 \pm 0.62	–	–
PLAN (Wang et al., 2025)	ICCV’25	✗	75.25 \pm 0.42	80.41 \pm 0.56	–	–	87.54 \pm 0.31	92.21 \pm 0.35	–	–
LoRA-P&M (Qiu et al., 2025)	NIPS’25	✗	79.95 \pm 0.18	85.29 \pm 0.93	<u>56.57</u> \pm 0.78	<u>65.35</u> \pm 1.81	88.45 \pm 0.35	92.89 \pm 1.13	<u>78.29</u> \pm 0.50	<u>83.39</u> \pm 0.61
CoSO (Cheng et al., 2025)	NIPS’25	✗	<u>81.10</u> \pm 0.39	<u>85.56</u> \pm 0.13	–	–	<u>88.77</u> \pm 0.16	<u>92.99</u> \pm 0.23	–	–
LoDA (Ours)	–	✗	81.93 \pm 0.20	86.90 \pm 0.40	62.59 \pm 0.64	70.87 \pm 1.61	90.47 \pm 0.06	93.46 \pm 1.42	81.74 \pm 0.78	89.35 \pm 0.98
SLCA (Zhang et al., 2023)	ICCV’23	✓	79.35 \pm 0.28	83.29 \pm 0.46	61.05 \pm 0.63	68.88 \pm 2.31	91.26 \pm 0.37	94.29 \pm 0.92	84.68 \pm 0.09	90.77 \pm 0.79
SSIAT (Tan et al., 2024)	CVPR’24	✓	79.38 \pm 0.59	83.63 \pm 0.43	62.43 \pm 1.63	70.83 \pm 1.63	91.35 \pm 0.26	94.35 \pm 0.60	88.75 \pm 0.38	93.00 \pm 0.90
VQ-Prompt (Jiao et al., 2024)	NIPS’24	✓	75.68 \pm 0.23	80.02 \pm 0.18	–	–	90.27 \pm 0.06	93.10 \pm 0.84	86.47 \pm 0.40	91.37 \pm 0.54
DIA (Li et al., 2025a)	CVPR’25	✓	79.03	85.61	61.69	<u>71.58</u>	90.80	94.29	86.73	93.21
MACIL (Wu et al., 2025a)	ICML’25	✓	<u>81.88</u> \pm 0.07	<u>85.95</u> \pm 0.27	<u>64.14</u> \pm 0.58	71.45 \pm 1.35	<u>91.94</u> \pm 0.17	<u>94.43</u> \pm 0.79	<u>90.52</u> \pm 0.13	<u>93.93</u> \pm 0.47
LoDA (Ours) + CA	–	✓	82.55 \pm 0.55	87.18 \pm 0.42	66.71 \pm 0.75	73.89 \pm 1.22	92.15 \pm 0.21	94.70 \pm 1.16	90.67 \pm 0.17	93.97 \pm 0.56

Table 2. Experimental results for 5 and 20 incremental sessions on ImageNetR, 20 sessions on ImageNetA, and 10 sessions on DomainNet.

Method	Venue	FR	5S-ImageNetR		20S-ImageNetR		20S-ImageNetA		10S-DomainNet	
			$\mathcal{A}_{Last} \uparrow$	$\mathcal{A}_{Avg} \uparrow$						
L2P (Wang et al., 2022b)	CVPR’22	✗	70.83 \pm 0.58	78.34 \pm 0.47	69.64 \pm 0.42	75.28 \pm 0.57	40.48 \pm 1.78	49.62 \pm 1.46	81.17 \pm 0.83	87.43 \pm 0.95
DualPrompt (Wang et al., 2022a)	ECCV’22	✗	73.05 \pm 0.50	79.47 \pm 0.40	66.61 \pm 0.58	72.45 \pm 0.37	42.28 \pm 1.94	53.39 \pm 1.64	81.70 \pm 0.78	87.80 \pm 0.99
CODAPrompt (Smith et al., 2023)	CVPR’23	✗	74.91 \pm 0.33	79.25 \pm 0.53	69.96 \pm 0.50	75.34 \pm 0.85	44.62 \pm 1.92	54.86 \pm 0.50	80.04 \pm 0.79	86.27 \pm 0.82
InfLoRA (Liang & Li, 2024)	CVPR’24	✗	77.52 \pm 0.37	82.01 \pm 0.12	71.01 \pm 0.45	77.28 \pm 0.45	46.81 \pm 2.30	57.13 \pm 0.95	81.45 \pm 0.68	87.55 \pm 0.57
SD-LoRA (Wu et al., 2025b)	ICLR-25	✗	79.15 \pm 0.20	83.01 \pm 0.42	75.26 \pm 0.37	80.22 \pm 0.72	49.12 \pm 1.78	59.63 \pm 1.57	81.01 \pm 0.42	86.85 \pm 0.40
Bi-LoRA (Zhu et al., 2025)	CVPR-25	✗	78.32 \pm 0.37	83.31 \pm 0.52	72.41 \pm 0.65	79.28 \pm 0.76	–	–	76.56 \pm 0.41	83.20 \pm 0.35
LoRA-P&M (Qiu et al., 2025)	NIPS-25	✗	81.47 \pm 0.56	85.96 \pm 0.52	76.37 \pm 0.69	82.77 \pm 0.31	<u>52.27</u> \pm 1.84	<u>62.15</u> \pm 1.33	<u>84.35</u> \pm 0.48	<u>89.43</u> \pm 0.27
CoSO (Cheng et al., 2025)	NIPS-25	✗	<u>82.10</u> \pm 0.13	<u>86.38</u> \pm 0.07	<u>78.19</u> \pm 0.28	<u>83.69</u> \pm 0.12	–	–	–	–
LoDA (Ours)	–	✗	83.37 \pm 0.14	87.46 \pm 0.41	78.96 \pm 0.23	84.94 \pm 0.17	55.74 \pm 1.89	65.54 \pm 2.43	85.49 \pm 0.11	90.15 \pm 0.42
SLCA (Zhang et al., 2023)	ICCV-23	✓	81.01 \pm 0.11	84.18 \pm 0.28	74.63 \pm 1.55	79.92 \pm 1.29	36.69 \pm 21.31	56.35 \pm 7.09	84.35 \pm 0.72	88.56 \pm 0.21
SSIAT (Tan et al., 2024)	CVPR-24	✓	80.52 \pm 0.07	84.25 \pm 0.31	75.67 \pm 0.24	82.30 \pm 0.36	59.16 \pm 1.03	<u>68.45</u> \pm 1.92	85.11 \pm 0.56	89.80 \pm 0.34
MACIL (Wu et al., 2025a)	ICML-25	✓	<u>83.37</u> \pm 0.26	<u>87.00</u> \pm 0.35	<u>79.43</u> \pm 0.34	<u>84.34</u> \pm 0.32	<u>59.36</u> \pm 1.27	68.03 \pm 2.00	<u>86.62</u> \pm 0.35	<u>90.88</u> \pm 0.20
LoDA (Ours) + CA	–	✓	83.69 \pm 0.38	87.45 \pm 0.42	81.13 \pm 0.42	86.26 \pm 0.20	64.47 \pm 1.27	72.30 \pm 1.78	87.33 \pm 0.36	91.40 \pm 0.17

$\mathbf{W}^1 + w_G \mathbf{B}_G \mathbf{A}_G$ on 10S-ImageNetA. A mild step along this direction does not harm and can even reduce the loss of Task-1, indicating positive knowledge transfer. However, fully adding Task-2’s optimum $w_G \mathbf{B}_G \mathbf{A}_G$ causes feature drifts and notably increases Task-1’s loss. This motivates our closed-form recalibration, which deduces optimal rescaling factors $\{\gamma^{(j)*}\}_{j=1}^r$ to reach a joint low-loss region for both old and new tasks.

For the isolated branch, its updates are highly beneficial for learning the new task, while previous tasks are insensitive to them. Therefore, we directly add them to the weights. The LoRA integration process is formulated as follows:

$$\mathbf{W}^t \leftarrow \mathbf{W}^{t-1} + w_G \mathbf{B}_G \mathbf{\Lambda}_G \mathbf{A}_G + \mathbf{B}_I \mathbf{A}_I, \quad (14)$$

where $\mathbf{\Lambda}_G$ is the diagonal rescaling matrix defined as $\mathbf{\Lambda}_G = \text{diag}(\gamma^{(1)*}, \dots, \gamma^{(j)*}, \dots, \gamma^{(r)*}) \in \mathbb{R}^{r \times r}$. During inference, we use only the updated backbone weight \mathbf{W}^t and discard all LoRA matrices, yielding an efficient inference stage with no extra parameters.

4. Experiments

Datasets and Evaluation Metrics. We evaluate our method on five datasets, namely ImageNetR (Hendrycks et al., 2021a), ImageNetA (Hendrycks et al., 2021b), CIFAR-100 (Krizhevsky et al., 2009), CUB (Wah et al., 2011) and DomainNet (Peng et al., 2019). ImageNet-R contains 30,000 images from 200 categories and diverse styles. ImageNet-A includes 7,500 real-world adversarial examples, spanning 200 classes. CIFAR-100 is a standard CL benchmark, including 60,000 32×32 images from 100 classes. DomainNet consists images from 345 classes across 6 visual domains. Following prior works (Gao et al., 2024), we select the top 200 most populous classes for evaluation.

Following existing PEFT-based methods (Tan et al., 2024; Wu et al., 2025a), we report results using 2 metrics: (1) Last accuracy (\mathcal{A}_{Last}), defined as the accuracy over all classes after the final session and (2) Average accuracy (\mathcal{A}_{Avg}), defined as the mean accuracy across all incremental sessions.

Implementation Details. All experiments are conducted on

Table 3. Ablation Studies on ImageNetR and ImageNetA datasets under 10 and 20 incremental sessions.

Idx	LoRA _G	LoRA _I	GAO	10S-ImageNetR		10S-ImageNetA		20S-ImageNetR		20S-ImageNetA	
				$\mathcal{A}_{Last} \uparrow$	$\mathcal{A}_{Avg} \uparrow$						
1	-	-	-	72.09 \pm 1.02	81.02 \pm 1.00	53.24 \pm 1.10	65.14 \pm 1.41	68.25 \pm 1.18	78.34 \pm 0.50	45.21 \pm 5.51	60.79 \pm 0.16
2	✓	-	-	79.19 \pm 0.26	85.18 \pm 0.94	59.62 \pm 1.87	68.84 \pm 2.45	76.59 \pm 0.39	83.26 \pm 0.70	51.70 \pm 0.31	62.23 \pm 1.74
3	-	✓	-	79.22 \pm 0.50	85.22 \pm 0.73	59.89 \pm 0.68	68.97 \pm 2.03	75.70 \pm 0.78	83.11 \pm 1.08	51.20 \pm 0.73	61.97 \pm 0.62
4	✓	✓	-	81.05 \pm 0.22	86.20 \pm 0.75	61.27 \pm 1.30	69.84 \pm 2.29	78.62 \pm 0.46	84.47 \pm 0.43	53.85 \pm 0.79	63.71 \pm 2.21
5	✓	✓	✓	81.93\pm0.20	86.91\pm0.40	62.59\pm0.64	70.87\pm1.61	78.96\pm0.23	84.94\pm0.17	55.74\pm1.89	65.54\pm2.43

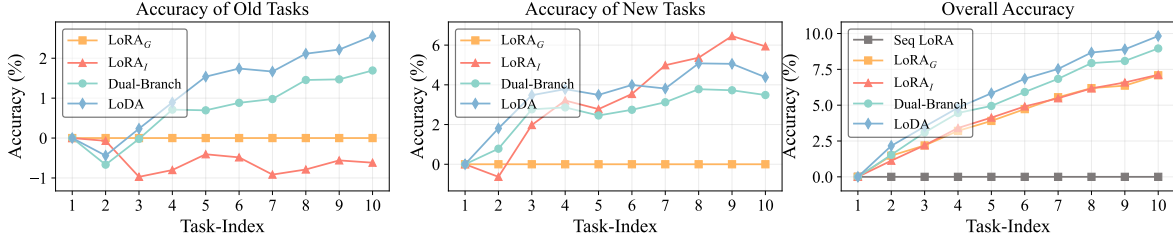


Figure 5. Relative accuracy curve of old tasks, new tasks and the overall performances on 10S-ImageNetR.

a single NVIDIA RTX 3090 GPU. We use ViT-B/16 (Dosovitskiy et al., 2021) pre-trained on ImageNet-21K (Rusakovsky et al., 2015) as the backbone. The model is optimized with an SGD optimizer with a Cosine Annealing scheduler. We train each task for 20 epochs with a batch size of 48. The initial learning rate is set to 0.02 for ImageNetR, 0.005 for CUB, and 0.01 for other datasets. Following (Wu et al., 2025a), we insert LoDA into all attention blocks with rank 32, and employ a cosine classifier for training the classification task. The hyper-parameters w_G in Eq.3 is set to 0.5 and λ in Eq.12 is set to 3.0. ρ_{max} for GAO is set to 0.7 for ImageNetR and 0.3 for other datasets.

LoDA+CA: an Enhanced Variant with Feature Replay. In PEFT-based continual learning, performance is often sensitive to the classifier design, particularly when Gaussian sampling-based feature replay is used. To isolate this factor and ensure fair comparison, we implement two protocols within the same framework: (1) **LoDA** follows the standard end-to-end training without any post-hoc classifier adjustment; (2) **LoDA+CA** is an enhanced variant that integrates the widely used Classifier Alignment (CA) technique (Zhang et al., 2023) into the training pipeline.

4.1. Comparison with the State-of-the-Arts

We compare LoDA with state-of-the-art PEFT-based approaches, including prompt-based methods (Wang et al., 2022b; Jiao et al., 2024; Wang et al., 2022a), adapter-based methods (Tan et al., 2024; Gao et al., 2023) and LoRA-based methods (Wang et al., 2025; Wu et al., 2025b; Liang & Li, 2024; Cheng et al., 2025; Qiu et al., 2025) on five CL benchmarks with various settings, as shown in Tab.1 and Tab.2. “FR” denotes the use of feature replay techniques.

The results demonstrate the superiority of our method. Without feature replay, LoDA consistently surpasses the strongest approach CoSO by 0.80%–1.70% in \mathcal{A}_{Last} . With

classifier alignment, LoDA+CA achieves the best performance across all settings, outperforming the feature replay-based SOTA MACIL by 0.15%–5.11% in \mathcal{A}_{Last} . Notably, the gains are substantial on the more challenging ImageNetA and ImageNetR datasets, where backbone features alone are insufficient for discrimination, but smaller on easier datasets such as CIFAR100 and CUB, where strong pre-trained representations reduce the need for backbone adaptation.

4.2. Ablation Studies

We conduct ablation studies on components of the LoDA framework, including the dual-branch LoRA module (*i.e.*, LoRA_G & LoRA_I) and the GAO training approach. The results are shown in Tab.3. We also built a naive baseline (Idx-1 in Tab. 3), which sequentially adapts the PTM using the standard single-branch LoRA module. To further analyze its effectiveness in balancing stability and plasticity, we visualize the accuracy curves of old tasks, the new task, and overall performance, as shown in Fig. 5.

The Effectiveness of the Dual-Branch LoRA. As shown in Tab. 3, LoRA_G (Idx-2) improves \mathcal{A}_{Last} by 6.49%–8.34% compared to baseline (Idx-1). It restricts adaptation to the task-shared subspace and approximates a feature-level joint optimum, which well balances performances on old and new tasks. LoRA_I (Idx-3) boosts \mathcal{A}_{Last} by 5.99%–7.45% by seeking updates that maximize gains on new task while minimizing interference with past tasks. Notably, enabling both LoRA_G and LoRA_I (Idx-4) further boosts \mathcal{A}_{Last} by 1.38%–2.15% over the best single-branch variant, highlighting their complementary roles. Fig.5 provides further evidence: (i) LoRA_G yields a stable shared update that accounts for performance over all tasks, reinforcing past knowledge; (ii) LoRA_I explores novel directions beyond old feature spaces and merges them intact into the backbone, integrating new knowledge and yielding higher new-task accuracy.

Table 4. Comparison with different subspace isolation methods.

Dataset	Method	$\mathcal{A}_{Last} \uparrow$	$\mathcal{A}_{Avg} \uparrow$
10S- ImageNetR	Random Orthogonal Bases	68.23 \pm 0.18	79.05 \pm 0.62
	Adam-NSCL (Wang et al., 2021)	74.50 \pm 0.77	82.29 \pm 1.12
	InfLoRA (Liang & Li, 2024)	75.15 \pm 0.37	82.57 \pm 0.84
	Relative Energy Maximization (Ours)	79.22\pm0.50	85.22\pm0.73
10S- ImageNetA	Random Orthogonal Bases	53.48 \pm 1.47	64.34 \pm 1.86
	Adam-NSCL (Wang et al., 2021)	55.95 \pm 1.84	66.94 \pm 2.03
	InfLoRA (Liang & Li, 2024)	57.10 \pm 0.96	67.55 \pm 1.94
	Relative Energy Maximization (Ours)	59.89\pm0.68	68.97\pm2.03

 Table 5. Comparison of our closed-form rescaling for LoRA_G with existing model merging strategies. ‘‘CoMA ($w = \alpha$)’’ denotes the result when setting the merge coefficient in CoMA to α .

Dataset	Strategy	$\mathcal{A}_{Last} \uparrow$	$\mathcal{A}_{Avg} \uparrow$
10S- ImageNetR	CoMA ($w = 0.1$) (Marouf et al., 2024)	76.93 \pm 0.65	81.89 \pm 0.95
	CoMA ($w = 0.3$) (Marouf et al., 2024)	78.39 \pm 0.78	84.48 \pm 1.01
	CoMA ($w = 0.5$) (Marouf et al., 2024)	77.95 \pm 0.55	84.30 \pm 0.90
	$\theta = \frac{t-1}{t}\theta_{t-1} + \frac{1}{t}\theta_t$ (Lin et al., 2022)	78.43 \pm 0.20	84.70 \pm 1.06
	Closed-Form Rescaling ($\lambda = 3.0$)	79.19\pm0.26	85.18\pm0.94
	Closed-Form Rescaling ($\lambda = 10.0$)	78.96\pm0.14	85.10\pm0.44
10S- ImageNetA	CoMA ($w = 0.1$) (Marouf et al., 2024)	58.11 \pm 0.97	66.97 \pm 2.15
	CoMA ($w = 0.3$) (Marouf et al., 2024)	58.84 \pm 0.67	68.46 \pm 1.98
	CoMA ($w = 0.5$) (Marouf et al., 2024)	57.84 \pm 1.41	68.01 \pm 1.56
	$\theta = \frac{t-1}{t}\theta_{t-1} + \frac{1}{t}\theta_t$ (Lin et al., 2022)	58.79 \pm 1.11	68.20 \pm 2.19
	Closed-Form Rescaling ($\lambda = 3.0$)	59.62\pm1.87	68.84\pm2.45
	Closed-Form Rescaling ($\lambda = 10.0$)	59.75\pm1.21	68.68\pm1.34

The Effectiveness of GAO. Building on the dual-branch structure, GAO further improves \mathcal{A}_{Last} by 0.34%–1.89%. As shown in Fig.5, it increases accuracy of both old and new tasks with larger improvements on old tasks. We attribute this to the regularization of gradient consistency, which filters out conflicting gradients early and yields more robust update directions that are less prone to future interference.

4.3. In-Depth Analysis

Comparison with other task isolation methods. To validate the rationality of constructing the isolated subspace by maximizing the relative projection energy $r(\mathbf{U})$, we compare the performance of LoRA_I (w/o LoRA_G) with existing task isolation methods, as shown in Tab.4. Adam-NSCL (Wang et al., 2021) and InfLoRA (Liang & Li, 2024) focus on directions that are weakly activated by past tasks while overlooking their activation on the new task, resulting in sub-optimal performances. In contrast, our objective (Eq.6) enforces a maximal activation contrast between the new and past tasks, deriving truly task-specific subspace.

Closed-Form Rescaling v.s. Existing Merging Strategies. We compare performance of LoRA_G (w/o LoRA_I) using our closed-form rescaling against existing merging strategies, as shown in Tab.5. Our feature-level objective in Eq.12 admits an exact closed-form solution that minimizes feature degradation from both past- and new-task optima, avoiding extra gradient computation (CoMA (Marouf et al., 2024)) and local linearity approximations. Moreover, we assign a unique rescaling factor for each rank-1 unit, which is more informative than direct averaging ($\theta = \frac{t-1}{t}\theta_{t-1} + \frac{1}{t}\theta_t$).

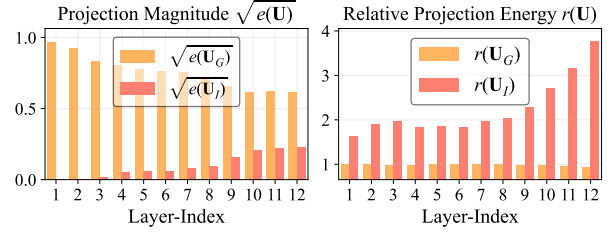


Figure 6. Projection magnitude and relative energy across different transformer layers on 10S-ImageNetA.

Table 6. Computational and storage overhead on 20S-ImageNetR.

Method	Training Stage		Inference Stage		
	Extra Memory	Training GFLOPs	Additional Params	Inference GFLOPs	\mathcal{A}_{Last}
InfLoRA (Liang & Li, 2024)	11.3MB	17.67	0.00M	17.60	71.01
SD-LoRA (Wu et al., 2025b)	14.1MB	20.51	0.00M	17.60	75.26
VPT-NSP (Lu et al., 2024)	28.4MB	17.72	0.09M	17.72	76.13
VPT-CPG (Lu et al., 2025)	28.4MB	17.72	1.66M	17.72	75.33
LoDA (Ours)	27.0MB	18.06	0.00M	17.60	78.96

Visualization and Analysis of the Projection Energy on Two Subspaces. We visualize normalized projection magnitude defined as $\sqrt{e(\mathbf{U})} = \sqrt{\|\mathbf{X}^t \mathbf{U}\|_F^2 / \|\mathbf{X}^t\|_F^2}$ of the current task onto the two subspaces, and the new-to-past relative projection energy $r(\mathbf{U})$ defined in Eq.5 on 10S-ImageNetA, as shown in Fig.6. \mathbf{U}_G dominates the projection energy across layers, indicating that most feature components lie in task-shared directions and providing evidence of strong task correlation. \mathbf{U}_I exhibits a larger projection and higher relative energy in deeper layers, suggesting that deeper layers emphasize more task-specific features.

Overhead Analysis. We report the computational and storage overhead of LoDA on 20S-ImageNetR in comparison with representative methods, as shown in Tab.6. LoDA incurs a modest storage overhead by maintaining the cumulative statistics $\mathbf{S}^{1:t-1} \in \mathbb{R}^{L \times (D \times D)}$ in L layers, which costs 27.0MB for ViT-B/16 with $L = 12$ and $D = 768$. This cost is *independent of the number of tasks*, thus scaling well to long task streams. LoDA introduces some training overhead (18.06 GFLOPs) due to the dual-branch LoRA, but incurs no extra parameters and overhead for inference (0.00M, 17.60 GFLOPs), while achieving the best performances.

5. Conclusion

In this work, we show that LoRA’s learning capability is governed by task feature projection onto its down-projection subspace, providing a principled way to control knowledge sharing & isolation in CL. Based on this insight, we propose LoDA, which decomposes the update space into general and truly isolated subspaces via two projection-energy-based objectives. LoDA then builds a dual-branch LoRA module that fixes down-projections on the decomposed bases and learns robust up-projections via Gradient-Aligned Optimization (GAO). After training, LoDA recalibrate the general branch

via a closed-form rescaling matrix to approximate a feature-level joint optimum. Overall, LoDA offers a novel view for CL, showing that subspace-aware adaptation provides an effective paradigm for stability-plasticity trade-off.

Impact Statement

This paper presents work whose goal is to advance the field of machine learning. There are many potential societal consequences of our work, none of which we feel must be specifically highlighted here.

References

- Cheng, Q., Wan, Y., Wu, L., Hou, C., and Zhang, L. Continuous subspace optimization for continual learning. In *Conference on Neural Information Processing Systems*, 2025.
- Dosovitskiy, A., Beyer, L., Kolesnikov, A., Weissenborn, D., Zhai, X., Unterthiner, T., Dehghani, M., Minderer, M., Heigold, G., Gelly, S., Uszkoreit, J., and Houslyby, N. An image is worth 16x16 words: Transformers for image recognition at scale. *ICLR*, 2021.
- Gao, Q., Zhao, C., Sun, Y., Xi, T., Zhang, G., Ghanem, B., and Zhang, J. A unified continual learning framework with general parameter-efficient tuning. In *Proceedings of the IEEE/CVF International Conference on Computer Vision*, pp. 11483–11493, 2023.
- Gao, Z., Cen, J., and Chang, X. Consistent prompting for rehearsal-free continual learning. In *Proceedings of the IEEE/CVF Conference on Computer Vision and Pattern Recognition*, pp. 28463–28473, 2024.
- Gargiulo, A. A., Crisostomi, D., Bucarelli, M. S., Scardapane, S., Silvestri, F., and Rodola, E. Task singular vectors: Reducing task interference in model merging. In *Proceedings of the Computer Vision and Pattern Recognition Conference*, pp. 18695–18705, 2025.
- Hendrycks, D., Basart, S., Mu, N., Kadavath, S., Wang, F., Dorundo, E., Desai, R., Zhu, T., Parajuli, S., Guo, M., et al. The many faces of robustness: A critical analysis of out-of-distribution generalization. In *Proceedings of the IEEE/CVF international conference on computer vision*, pp. 8340–8349, 2021a.
- Hendrycks, D., Zhao, K., Basart, S., Steinhardt, J., and Song, D. Natural adversarial examples. In *Proceedings of the IEEE/CVF conference on computer vision and pattern recognition*, pp. 15262–15271, 2021b.
- Hu, E. J., Shen, Y., Wallis, P., Allen-Zhu, Z., Li, Y., Wang, S., Wang, L., and Chen, W. LoRA: Low-rank adaptation of large language models. In *International Conference on Learning Representations*, 2022. URL <https://openreview.net/forum?id=nZeVKeeFYf9>.
- Ilharco, G., Ribeiro, M. T., Wortsman, M., Gururangan, S., Schmidt, L., Hajishirzi, H., and Farhadi, A. Editing models with task arithmetic. In *The Eleventh International Conference on Learning Representations (ICLR)*, 2023. URL <https://openreview.net/forum?id=6t0Kwf8-jrj>.
- Jiao, L., Lai, Q., Li, Y., and Xu, Q. Vector quantization prompting for continual learning. *NeurIPS*, 2024.
- Kim, D. and Han, B. On the stability-plasticity dilemma of class-incremental learning. In *Proceedings of the IEEE/CVF Conference on Computer Vision and Pattern Recognition*, pp. 20196–20204, 2023.
- Kirkpatrick, J., Pascanu, R., Rabinowitz, N., Veness, J., Desjardins, G., Rusu, A. A., Milan, K., Quan, J., Ramalho, T., Grabska-Barwinska, A., et al. Overcoming catastrophic forgetting in neural networks. *Proceedings of the national academy of sciences*, 114(13):3521–3526, 2017.
- Krizhevsky, A., Hinton, G., et al. Learning multiple layers of features from tiny images. 2009.
- Li, J., Wang, S., Qian, B., He, Y., Wei, X., Wang, Q., and Gong, Y. Dynamic integration of task-specific adapters for class incremental learning. In *Proceedings of the Computer Vision and Pattern Recognition Conference*, pp. 30545–30555, 2025a.
- Li, M., Lu, Y., Dai, Q., Huang, S., Ding, Y., and Lu, H. Be-came: Bayesian continual learning with adaptive model merging. In *International Conference on Machine Learning*, 2025b.
- Liang, Y.-S. and Li, W.-J. Inflora: Interference-free low-rank adaptation for continual learning. In *Proceedings of the IEEE/CVF Conference on Computer Vision and Pattern Recognition*, pp. 23638–23647, 2024.
- Lin, G., Chu, H., and Lai, H. Towards better plasticity-stability trade-off in incremental learning: A simple linear connector. In *Proceedings of the IEEE/CVF conference on computer vision and pattern recognition*, pp. 89–98, 2022.
- Lu, Y., Zhang, S., Cheng, D., Xing, Y., Wang, N., Wang, P., and Zhang, Y. Visual Prompt Tuning in Null Space for Continual Learning. In *Conference on Neural Information Processing Systems*, 2024.
- Lu, Y., Zhang, S., Cheng, D., Liang, G., Xing, Y., Wang, N., and Zhang, Y. Training consistent mixture-of-experts-based prompt generator for continual learning. In *Proceedings of the AAAI Conference on Artificial Intelligence*, volume 39, pp. 19152–19160, 2025.

- Marouf, I. E., Roy, S., Tartaglione, E., and Lathuilière, S. Weighted ensemble models are strong continual learners, 2024.
- Ortiz-Jimenez, G., Favero, A., and Frossard, P. Task arithmetic in the tangent space: Improved editing of pre-trained models. *Advances in Neural Information Processing Systems*, 36:66727–66754, 2023.
- Peng, X., Bai, Q., Xia, X., Huang, Z., Saenko, K., and Wang, B. Moment matching for multi-source domain adaptation. In *Proceedings of the IEEE/CVF international conference on computer vision*, pp. 1406–1415, 2019.
- Qiao, J., Tan, X., Chen, C., Qu, Y., Peng, Y., Xie, Y., et al. Prompt gradient projection for continual learning. In *The Twelfth International Conference on Learning Representations*, 2023.
- Qiu, H., Zhang, M., Qiao, Z., and Nie, L. Train with perturbation, infer after merging: A two-stage framework for continual learning. In *Conference on Neural Information Processing Systems*, 2025.
- Russakovsky, O., Deng, J., Su, H., Krause, J., Satheesh, S., Ma, S., Huang, Z., Karpathy, A., Khosla, A., Bernstein, M., et al. Imagenet large scale visual recognition challenge. *International journal of computer vision*, 115: 211–252, 2015.
- Smith, J. S., Karlinsky, L., Gutta, V., Cascante-Bonilla, P., Kim, D., Arbelles, A., Panda, R., Feris, R., and Kira, Z. Coda-prompt: Continual decomposed attention-based prompting for rehearsal-free continual learning. In *Proceedings of the IEEE/CVF Conference on Computer Vision and Pattern Recognition*, pp. 11909–11919, 2023.
- Stoica, G., Ramesh, P., Ecsedi, B., Choshen, L., and Hoffman, J. Model merging with svd to tie the knots. *ICLR*, 2025.
- Tan, Y., Zhou, Q., Xiang, X., Wang, K., Wu, Y., and Li, Y. Semantically-shifted incremental adapter-tuning is a continual vitransformer. In *Proceedings of the IEEE/CVF Conference on Computer Vision and Pattern Recognition*, pp. 23252–23262, 2024.
- Wah, C., Branson, S., Welinder, P., Perona, P., and Belongie, S. The caltech-ucsd birds-200-2011 dataset. 2011.
- Wang, S., Li, X., Sun, J., and Xu, Z. Training networks in null space of feature covariance for continual learning. In *Proceedings of the IEEE/CVF conference on Computer Vision and Pattern Recognition*, pp. 184–193, 2021.
- Wang, X., Chen, T., Ge, Q., Xia, H., Bao, R., Zheng, R., Zhang, Q., Gui, T., and Huang, X.-J. Orthogonal subspace learning for language model continual learning. In *Findings of the Association for Computational Linguistics: EMNLP 2023*, pp. 10658–10671, 2023.
- Wang, X., Zhuang, Z., and Zhang, Y. Plan: Proactive low-rank allocation for continual learning. In *Proceedings of the IEEE/CVF International Conference on Computer Vision*, pp. 2909–2918, 2025.
- Wang, Z., Zhang, Z., Ebrahimi, S., Sun, R., Zhang, H., Lee, C.-Y., Ren, X., Su, G., Perot, V., Dy, J., et al. Dualprompt: Complementary prompting for rehearsal-free continual learning. In *European Conference on Computer Vision*, pp. 631–648. Springer, 2022a.
- Wang, Z., Zhang, Z., Lee, C.-Y., Zhang, H., Sun, R., Ren, X., Su, G., Perot, V., Dy, J., and Pfister, T. Learning to prompt for continual learning. In *Proceedings of the IEEE/CVF conference on computer vision and pattern recognition*, pp. 139–149, 2022b.
- Wu, F., Cheng, L., Tang, S., Zhu, X., Fang, C., Zhang, D., and Wang, M. Navigating semantic drift in task-agnostic class-incremental learning. In *Forty-second International Conference on Machine Learning*, 2025a.
- Wu, Y., Piao, H., Huang, L.-K., Wang, R., Li, W., Pfister, H., Meng, D., Ma, K., and Wei, Y. SD-loRA: Scalable decoupled low-rank adaptation for class incremental learning. In *The Thirteenth International Conference on Learning Representations*, 2025b. URL <https://openreview.net/forum?id=5U1rlpX68A>.
- Zhang, G., Wang, L., Kang, G., Chen, L., and Wei, Y. Slca: Slow learner with classifier alignment for continual learning on a pre-trained model. In *Proceedings of the IEEE/CVF International Conference on Computer Vision*, pp. 19148–19158, 2023.
- Zhu, H., Zhang, Y., Dong, J., and Koniusz, P. Bilora: Almost-orthogonal parameter spaces for continual learning. In *Proceedings of the Computer Vision and Pattern Recognition Conference*, pp. 25613–25622, 2025.